CPT-Based Probabilistic Characterization of Three-Dimensional Spatial Variability Using MLE

Te Xiao, S.M.ASCE[1]; Dian-Qing Li, Ph.D., M.ASCE[2]; Zi-Jun Cao, Ph.D., M.ASCE[3]; and Li-Min Zhang, Ph.D., F.ASCE[4]

Abstract: Engineering geological characterization, subject to spatial variability of soil properties, is a three-dimensional (3D) problem in reality, although it is often simplified as one- or two-dimensional. Direct characterization of 3D spatial variability is a challenging task due to the scarcity of geotechnical data and a satisfactory characterization method. To address such a problem, this paper develops a cone penetration test (CPT)–based probabilistic approach for characterizing 3D spatial variability underlying the framework of maximum likelihood estimation (MLE). A matrix decomposition technique is applied to enhance the practical application of MLE for high-dimensional and spatially correlated data. Results of a case study and three virtual site analyses indicate that MLE provides more accurate estimates of random field parameters with smaller statistical uncertainty than the commonly used method of moments with best fitting, particularly for the estimation of scale of fluctuation. In addition, simultaneous vertical and horizontal characterization based on multiple CPTs is a feasible way for 3D spatial variability characterization in the presence of limited data, such as the limited sounding issue and the thin layer issue. The sampling strategy having some closely located CPTs is preferable for 3D spatial variability characterization. **DOI: 10.1061/(ASCE)GT.1943-5606.0001875.**

Author keywords: Site characterization; Three-dimensional spatial variability; Random field; Maximum likelihood estimation; Cone penetration test.

Introduction

As one of major sources of geotechnical uncertainties, the spatial variability of soil properties has significant effects on the reliability of geotechnical structures (Fenton and Griffiths 2008; Li et al. 2016a, b; Xiao et al. 2016, 2017a). It is well recognized to be three-dimensional (3D) and preserve anisotropy in vertical and horizontal directions owing to various natural processes (Phoon and Kulhawy 1999). To completely consider effects of spatially varying soils, probabilistic characterization of 3D spatial variability is essential, in which spatial variability is often described by random field theory (Vanmarcke 2010) and quantified by several parameters (i.e., trend, standard deviation, and scale of fluctuation). Nevertheless, the 3D spatial variability characterization is a challenging task and is rarely implemented in an explicit manner (Kulatilake and Miller 1987; Pardo-Igúzquiza and Dowd 1997) for at least two reasons: (1) physically, the lack of site investigation data in geotechnical practice (Wang et al. 2016; Phoon 2017), and (2) mathematically, the lack of a satisfactory characterization method. For simplicity, most studies decompose the 3D spatial variability into vertical and horizontal components, and simplify the 3D characterization as two individual parts, including vertically along the depth of the borehole or sounding (Fenton 1999a; Wang et al. 2010) and horizontally in a transverse plane (Tang 1979; DeGroot and Baecher 1993). Such treatment cannot make full use of the information contained in limited data.

Cone penetration test (CPT) is the most widely used site investigation approach for vertical spatial variability characterization because it provides a nearly continuous data profile. The limited data issue is, however, still inevitable in the case of thin soil layers (Ching et al. 2016b). In contrast, the scarcity of test soundings, for a majority of projects, leads to limited data pairs in the transverse plane and makes the characterization of horizontal spatial variability more difficult. For example, Table 1 summaries 24 studies on horizontal spatial variability characterization using CPT in the last four decades. The typical number of test soundings is limited, ranging from 10–30. The estimated horizontal scale of fluctuation varies from 0.14 to approximately 600 m, whose large variation, compared with that reported by Phoon and Kulhawy (1999), may be attributed to the natural site diversity, test scales (e.g., site scale and sounding distance), and data processing procedures (e.g., detrending, normalizing, and averaging). In the presence of limited data, estimates of random field parameters would be sensitive to these factors and, more essentially, be relatively inaccurate with a large statistical uncertainty. The statistical uncertainty affects the reliability of geotechnical structures as well (Ching et al. 2016a) and needs a quantitative evaluation.

Several approaches are available to infer random field parameters in spatial variability characterization, such as the method of moments with best fitting (MMBF) (Tang 1979; Lacasse and Nadim 1996; Uzielli et al. 2005; Zhang and Dasaka 2010), maximum likelihood estimation (MLE) (DeGroot and Baecher 1993;

[1]Ph.D. Candidate, State Key Laboratory of Water Resources and Hydropower Engineering Science, Wuhan Univ., 8 Donghu South Rd., Wuhan 430072, P.R. China. E-mail: short_xiaote@whu.edu.cn

[2]Professor, State Key Laboratory of Water Resources and Hydropower Engineering Science, Wuhan Univ., 8 Donghu South Rd., Wuhan 430072, P.R. China (corresponding author). E-mail: dianqing@whu.edu.cn

[3]Associate Professor, State Key Laboratory of Water Resources and Hydropower Engineering Science, Wuhan Univ., 8 Donghu South Rd., Wuhan 430072, P.R. China. E-mail: zijuncao@whu.edu.cn

[4]Professor, Dept. of Civil and Environmental Engineering, Hong Kong Univ. of Science and Technology, Clear Water Bay, Kowloon, Hong Kong. E-mail: cezhangl@ust.hk

Note. This manuscript was submitted on March 20, 2017; approved on November 8, 2017; published online on March 10, 2018. Discussion period open until August 10, 2018; separate discussions must be submitted for individual papers. This paper is part of the ***Journal of Geotechnical and Geoenvironmental Engineering***, © ASCE, ISSN 1090-0241.

Table 1. Summary on Horizontal Spatial Variability Characterization Using CPT

Identifier	Soil type	CPT parameter[a]	Number of soundings	Maximum site scale (m)	Minimum sounding distance (m)	Horizontal scale of fluctuation (m)	Method[b]	Reference
1	Sand and clay	q_c	30	200	15	35–62[c]	MMBF (CF)	Tang (1979)
2	Sand and silt	q_c	—	—	—	20	—	Phoon et al. (1995)
3	Marine clay	q_t	—	—	—	23–66	—	Phoon et al. (1995)
4	Sand and silt	q_c	—	—	—	37	—	Phoon et al. (1995)
5	Fine sand	q_c	24	350	15	13	MMBF (VF)	Wu et al. (1987)
6	Offshore sand	q_c	17	250	10	25–67[c]	MMBF (CF)	Lacasse and Nadim (1996)
7	—	q_c	—	—	—	42–80	—	Phoon et al. (1995)
8	Clay	q_c	222	50	0.5	2.8–3.3[c]	MMBF (SF)	Jaksa (1995)
9	Clay	q_c	1[d]	7.62	0.05	0.14	MMBF (SF)	Jaksa (1995)
10	Alluvial deposit	q_c	12	70	1	1.1–3.9	MMBF (SF)	O'Neil and Yoon (2003)
11	Sand	q_c, f_s	22	—	—	2–25, 7–19	MMBF (CF)	Akkaya and Vanmarcke (2003)
12	Clay	q_c, f_s	24	—	—	2.5–30, 2–14	MMBF (CF)	Akkaya and Vanmarcke (2003)
13	Sand	q_a	36	250	2	22–34	Bayesian	Vrouwenvelder and Calle (2003)
14	Sand, silt, and clay	q_c, f_s	71	5,000	20	100–200	MMBF (CF)	Liu and Chen (2006)
15	Sand, silt, and clay	q_c, f_s	71	5,000	—	286–597, 287–555	MMBF (CF)	Liu and Chen (2010)
16	Clay and silt clay	q_c	42, 38	1,700	50	283, 225	MMBF (VF)	Ng and Zhou (2010)
17	Clay	q_t	9	26	6	3.0–9.9	MMVSM	Stuedlein et al. (2012)
18	Sand	q_c	18	45	1.5	1.7–15.9	MMBF (CF)	Lloret-Cabot et al. (2014)
19	Sand	$q_{c1\,N}$, F_r	9	40	10	2.4, 2.8[c]	MMBF (CF)	Firouzianbandpey et al. (2014)
20	Sand	$q_{c1\,N}$, F_r	12	23	2	4.0, 2.4[c]	MMBF (CF)	Firouzianbandpey et al. (2014)
21	Clay	q_{net}	16	200	10	20	MMBF (CF)	Müller et al. (2013)
22	Sand and clay	q_n	333	5,500	9	12.2–16.1	MMBF (CF)	Bombasaro and Kasper (2016)
23	Clay-bound sand	q_a	29	30	6	6–13	MMBF (CF)	Lingwanda et al. (2017)
24	Alluvial deposit	q_{c1N}	16	7	1	1.1–1.5	MMVSM	Cai et al. (2017)

[a]f_s = sleeve friction; q_a = average penetration resistance; q_c = cone tip resistance; q_t = corrected cone tip resistance; q_{net} = net corrected cone tip resistance; q_{c1N} and q_n = normalized cone tip resistance; and F_r = normalized friction ratio.
[b]CF = correlation or covariance function fitting; VF = variance reduction function fitting; SF = semivariogram or variogram fitting; and MMVSM = method of moments with Vanmarcke's simplified method.
[c]Converted from autocorrelation distance.
[d]Custom-designed horizontal CPT.

Fenton 1999a, b), and Bayesian approach (Wang et al. 2010; Cao and Wang 2013, 2014; Tian et al. 2016). Compared with the most popular MMBF, MLE has the advantages (Baecher et al. 1999) of being (1) a standardized procedure for parameter inference, particularly for scale of fluctuation; (2) capable of evaluating associated statistical uncertainty; and (3) compatible with Bayesian philosophy. However, MLE suffers from a high computational burden when high-dimensional and spatially correlated data are applied (Pardo-Igúzquiza and Dowd 1997; Stein et al. 2004), such as the data collected from multiple CPTs within a site. This mathematical problem restricts the amount of data in 3D spatial variability characterization and, in turn, intensifies the limited data issue.

This study aims to develop a CPT-based probabilistic approach for characterizing 3D spatial variability. The vertical and horizontal spatial variabilities are characterized simultaneously, underlying a uniform framework of MLE, to take full advantage of all information in the presence of limited data. The high-dimensional problem hindering the practical application of MLE is addressed by a matrix decomposition technique. Finally, the approach is illustrated and validated using a case study and several virtual site analyses.

Characterization of 3D Spatial Variability

Three-Dimensional Spatial Variability Modeling

To account for the impact of effective overburden stress, the normalized CPT data [i.e., normalized cone tip resistance (Q_{tn}) and normalized friction ratio (F_r)] (Robertson 2009) rather than raw ones were utilized for 3D spatial variability characterization. For simplicity, let $\boldsymbol{X}$ be an $n \times 1$ vector of CPT data, where n = number of readings. The measured X values at different locations can be decomposed into a smoothly varying trend and a fluctuating residual (ε) as (Baecher and Christian 2003)

$$\boldsymbol{X} = \boldsymbol{F}\boldsymbol{\beta} + \boldsymbol{\varepsilon} \tag{1}$$

where $\boldsymbol{F}$ and $\boldsymbol{\beta}$ = trend function matrix and coefficient vector, respectively. Considering a 3D linear trend function $X = \beta_0 + \beta_x x + \beta_y y + \beta_z z$, for example, $\boldsymbol{F}$ is an $n \times 4$ matrix with each row of $[1, x_i, y_i, z_i]$ and $\boldsymbol{\beta} = [\beta_0, \beta_x, \beta_y, \beta_z]^T$, in which (x_i, y_i, z_i), $i = 1, 2, \ldots, n$, is the absolute position of the ith reading. As a rule of thumb, ε is often assumed to be jointly normally distributed in space and quantified by a standard deviation (σ) and a decaying spatial correlation function related to the relative position using random field theory (Vanmarcke 2010). For example, a 3D single-exponential correlation function is defined as

$$\rho = \exp\left(-2\sqrt{\tau_x^2 + \tau_y^2}\Big/\delta_h - 2\tau_z/\delta_v\right) \tag{2}$$

where ρ = correlation coefficient between X values at two locations with relative distance (τ_x, τ_y, τ_z) in x (horizontal), y (horizontal), and z (vertical) directions; and δ_h and δ_v = horizontal and vertical scales of fluctuation, respectively. Herein, isotropic horizontal spatial variability is assumed because the horizontal anisotropy is difficult to capture through limited data. Eventually, the 3D spatial variability is described by a set of random field parameters $\boldsymbol{\theta} = (\boldsymbol{\beta}, \sigma, \delta_v, \delta_h)$, which is inferred using MLE in the following section.

Maximum Likelihood Estimation

According to the spatial variability model [i.e., Eq. (1)], the likelihood of observing the sequence of observations $\boldsymbol{X}$ for a given set of $\boldsymbol{\theta}$ can be logarithmically written as (DeGroot and Baecher 1993; Fenton 1999a)

$$\ln L(\boldsymbol{X}|\boldsymbol{\theta}) = -\frac{n}{2}\ln(2\pi) - \frac{n}{2}\ln\sigma^2 - \frac{1}{2}\ln|\boldsymbol{R}| - \frac{1}{2\sigma^2}(\boldsymbol{X} - \boldsymbol{F}\boldsymbol{\beta})^{\mathrm{T}}\boldsymbol{R}^{-1}(\boldsymbol{X} - \boldsymbol{F}\boldsymbol{\beta}) \tag{3}$$

where $\boldsymbol{R} = [\rho] = n \times n$ global correlation matrix with elements calculated by Eq. (2). In the context of MLE, estimates of $\boldsymbol{\theta}$ are determined by maximizing the log-likelihood function. Particularly, estimates of $\boldsymbol{\beta}$ and σ are obtained through differentiation as

$$\hat{\boldsymbol{\beta}} = (\boldsymbol{F}^{\mathrm{T}}\boldsymbol{R}^{-1}\boldsymbol{F})^{-1}\boldsymbol{F}^{\mathrm{T}}\boldsymbol{R}^{-1}\boldsymbol{X} \tag{4}$$

$$\hat{\sigma}^2 = \frac{1}{n}\boldsymbol{E}^{\mathrm{T}}\boldsymbol{R}^{-1}\boldsymbol{E} \tag{5}$$

where $\boldsymbol{E} = \boldsymbol{X} - \boldsymbol{F}\hat{\boldsymbol{\beta}}$. These estimates are similar to moment-based ones, but extra effort was made to consider correlations. Because closed forms of differentiating $|\boldsymbol{R}|$ and $\boldsymbol{R}^{-1}$ with respect to δ_v and δ_h do not exist (Fenton 1999a), estimates of δ_v and δ_h were determined alternatively via optimization techniques. Substituting Eqs. (4) and (5) into Eq. (3) and removing constant terms give the so-called profile likelihood function as (Fenton 1999a)

$$L_p(\boldsymbol{X}|\boldsymbol{\theta}) = -\frac{n}{2}\ln\hat{\sigma}^2 - \frac{1}{2}\ln|\boldsymbol{R}| \tag{6}$$

Maximizing Eq. (6) instead of Eq. (3) requires only two parameters (i.e., δ_v and δ_h) to be optimized and enhances the application of gradient- or grid-based optimization in MLE. In this study, a pseudo-global-optimization technique with multiple random initial values was applied. The procedure is summarized as follows:

1. Assume an initial set of δ_v and δ_h;
2. Generate correlation matrix $\boldsymbol{R}$ based on Eq. (2) and compute $\ln|\boldsymbol{R}|$ and $\boldsymbol{R}^{-1}$;
3. Obtain $\hat{\boldsymbol{\beta}}$ and $\hat{\sigma}^2$ using Eqs. (4) and (5) and calculate $L_p(\boldsymbol{X}|\boldsymbol{\theta})$ using Eq. (6);
4. Move to next set of δ_v and δ_h and repeat Steps 2–4 until a local maximum of $L_p(\boldsymbol{X}|\boldsymbol{\theta})$ is found;
5. Repeat Steps 2–4 with different initial sets of δ_v and δ_h so that multiple local maxima of $L_p(\boldsymbol{X}|\boldsymbol{\theta})$ are obtained;
6. Choose the largest local maximum as the global maximum and corresponding estimates as the maximum likelihood estimates $\hat{\boldsymbol{\theta}}$.

Notably, calculation of $\ln|\boldsymbol{R}|$ and $\boldsymbol{R}^{-1}$ in Step 2 required intensive computational efforts for high-dimensional data (i.e., very large n), as did other $\boldsymbol{R}^{-1}$-related calculations (e.g., calculation of $\boldsymbol{\beta}$ and σ in Step 3). This computational difficulty was a major issue that hindered the practical application of MLE in 3D spatial variability characterization, which will be addressed in the next section.

Decomposition of Global Correlation Matrix

Consider, for example, that 40 CPTs at a penetration interval of 20 mm and a depth of 20 m provide $n = 40 \times 20/0.02 = 40{,}000$ data records, leading to a high-dimensional correlation matrix $\boldsymbol{R}$ (i.e., $40{,}000 \times 40{,}000$ in size). It is not trivial to repeatedly compute $\ln|\boldsymbol{R}|$ and $\boldsymbol{R}^{-1}$ during the optimization.

Fortunately, if data records are deliberately arranged one sounding after another, the global correlation matrix can be decomposed into several smaller correlation matrices. Provided that each CPT has a uniform interval and a consistent depth, as shown in

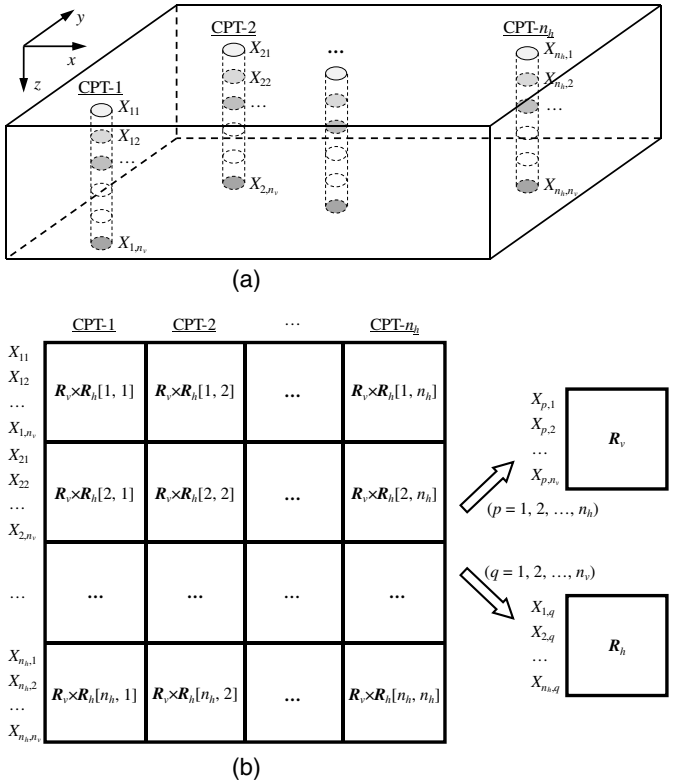

Fig. 1. Spatial distribution and correlation of CPT data: (a) spatial distribution of CPT data; (b) structure of global correlation matrix

Fig. 1(a), the arranged data $\boldsymbol{X} = [X_{11}, X_{12}, \ldots, X_{1,n_v}, X_{21}, X_{22}, \ldots, X_{2,n_v}, \ldots, X_{n_h,1}, X_{n_h,2}, \ldots, X_{n_h,n_v}]^T$, where n_v = number of data within a sounding, n_h = number of soundings, and $n_v \times n_h = n$. For instance, $n_v = 1{,}000$ and $n_h = 40$ in the previous example and $n_v \gg n_h$ due to the nature of CPT. By this means, the global correlation matrix $\boldsymbol{R}$ is a block matrix as shown in Fig. 1(b) and can be decomposed as $\boldsymbol{R} = \boldsymbol{R}_h \otimes \boldsymbol{R}_v$, where $\otimes$ = Kronecker product, $\boldsymbol{R}_v$ = vertical correlation matrix for data within a sounding, and $\boldsymbol{R}_h$ = horizontal correlation matrix for data at the same depth. By virtue of the Kronecker product, $|\boldsymbol{R}|$ and $\boldsymbol{R}^{-1}$ need not be directly calculated, but are given as

$$\ln |\boldsymbol{R}| = n_v \ln |\boldsymbol{R}_h| + n_h \ln |\boldsymbol{R}_v| \tag{7}$$

$$\boldsymbol{R}^{-1} = \boldsymbol{R}_h^{-1} \otimes \boldsymbol{R}_v^{-1} \tag{8}$$

Calculations for determinants and inverses of $\boldsymbol{R}_v$ and $\boldsymbol{R}_h$ are much easier than those of $\boldsymbol{R}$. For the single-exponential correlation function with a uniform interval of CPT in particular, an analytical solution was available to efficiently compute $|\boldsymbol{R}_v|$ and $\boldsymbol{R}_v^{-1}$ (Fenton 1999a). With regard to $\boldsymbol{R}_h$, direct computation was quite simple due to its naturally small matrix size. In addition, the assembly of $\boldsymbol{R}^{-1}$ in Eq. (8) was possibly avoided to save computational memory and further improve computational efficiency. For example, the $\boldsymbol{R}^{-1}$-related matrix multiplication in Eq. (5) and elsewhere can be calculated, according to the lemma of Kronecker product given in Appendix I, as

$$\boldsymbol{E}^{\mathrm{T}} \boldsymbol{R}^{-1} \boldsymbol{E} = \mathrm{tr}[\underline{\boldsymbol{E}}^{\mathrm{T}} \boldsymbol{R}_v^{-1} \underline{\boldsymbol{E}} (\boldsymbol{R}_h^{-1})^{\mathrm{T}}] \tag{9}$$

where $\underline{\boldsymbol{E}} = n_v \times n_h$ reordered matrix of $\boldsymbol{E}$; and $\mathrm{tr}(\cdot)$ = trace of a matrix. Therefore, by decomposing the global correlation matrix into smaller vertical and horizontal correlation matrices, the computational effort for 3D spatial variability characterization using MLE was almost comparable with that for one-dimensional vertical spatial variability characterization.

Statistical Uncertainty of Inferred Parameters

As previously mentioned, MLE has the ability to provide statistical uncertainty on inferred parameters in the form of covariance $\mathrm{C}(\hat{\boldsymbol{\theta}})$. By definition, $\mathrm{C}(\hat{\boldsymbol{\theta}})$ approximately and asymptotically equals the inverse of the Fisher information matrix. In practice, it is more frequently estimated by the inverse of observed information matrix evaluated at maximum likelihood estimates $\hat{\boldsymbol{\theta}}$ (Pawitan 2001)

$$\mathrm{C}(\hat{\boldsymbol{\theta}}) \approx \left[-\frac{\partial^2}{\partial \boldsymbol{\theta}^2} \ln L(\boldsymbol{X}|\boldsymbol{\theta}) \bigg|_{\boldsymbol{\theta}=\hat{\boldsymbol{\theta}}} \right]^{-1} \tag{10}$$

Regarding to log-likelihood function defined in Eq. (3), calculation of second-order partial derivatives was derived in a semianalytical manner, as provided in Appendix II. For fair comparison, the statistical uncertainty was normalized in the form of the coefficient of variance (COV) in this study. The influence of limited data on statistical uncertainties of different random field parameters will be explored through virtual site analysis subsequently.

Applications to 3D Random Field Simulation and Spatial Interpolation

Once random field parameters are obtained through 3D spatial variability characterization, geotechnical engineers still need to extend the knowledge from a few investigated locations (including random field parameters and soil properties) to the whole site. From a probabilistic perspective, this can be achieved by 3D random field simulation and spatial interpolation.

Various random field generation techniques have been developed in the past few decades (Fenton and Griffiths 2008), among which the covariance matrix decomposition approach (typically through Cholesky decomposition) is the most widely used because of its simplicity (Wang et al. 2010; Ching et al. 2016b; Li et al. 2016a, b). In the context of the covariance matrix decomposition approach, an $n \times 1$ standard normal random field $\mathbf{Z}$ can be produced by

$$\boldsymbol{Z} = \boldsymbol{L}\boldsymbol{U} \tag{11}$$

where $\boldsymbol{U} = n \times 1$ independent standard normal random vector; and $\boldsymbol{L} = n \times n$ lower triangular matrix satisfying $\boldsymbol{L}\boldsymbol{L}^T = \boldsymbol{R}$. This approach is, however, rarely applied to 3D random field simulation because the direct Cholesky decomposition of high-dimensional $\boldsymbol{R}$ is both time-consuming and prone to considerable round-off error (Fenton and Griffiths 2008). Considering that $\boldsymbol{R} = \boldsymbol{R}_h \otimes \boldsymbol{R}_v$, it is easy to prove that $\boldsymbol{L} = \boldsymbol{L}_h \otimes \boldsymbol{L}_v$, where $\boldsymbol{L}_h$ and $\boldsymbol{L}_v$ = lower triangular matrices satisfying $\boldsymbol{L}_h \boldsymbol{L}_h^T = \boldsymbol{R}_h$ and $\boldsymbol{L}_v \boldsymbol{L}_v^T = \boldsymbol{R}_v$, respectively. The existence of $\boldsymbol{L}$ guarantees the positive definiteness of $\boldsymbol{R}$ formed by Eq. (2) in turn. Applying the lemma of the Kronecker product given in Appendix I, Eq. (11) is equivalent to

$$\underline{\boldsymbol{Z}} = \boldsymbol{L}_v \underline{\boldsymbol{U}} \boldsymbol{L}_h^{\mathrm{T}} \tag{12}$$

where $\underline{\boldsymbol{U}}$ and $\underline{\boldsymbol{Z}} = n_v \times n_h$ reordered matrices of $\boldsymbol{U}$ and $\boldsymbol{Z}$, respectively. With the aid of Eq. (12), the covariance matrix decomposition approach can be easily applied to 3D random field simulation with both high efficiency and accuracy. A simple example of 3D random field realization is shown in Fig. 2, which contains $n = 50 \times 50 \times 1{,}000 = 2.5 \times 10^6$ elements in total but takes only

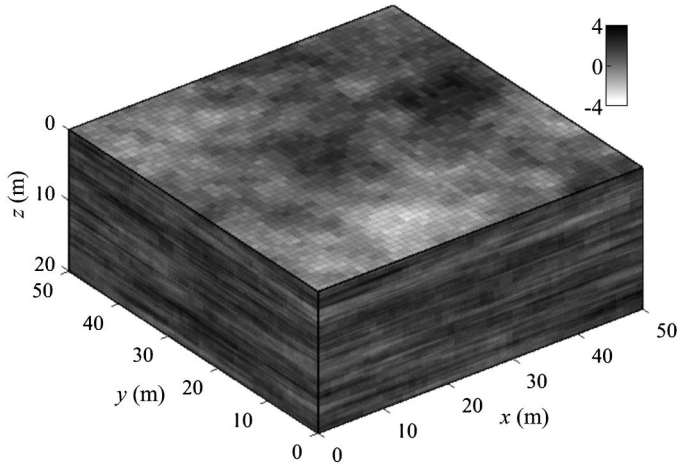

Fig. 2. Example of 3D random field realization (50 × 50 × 1,000)

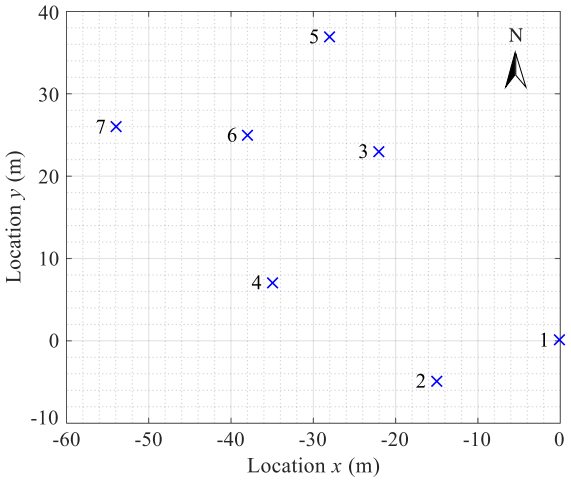

Fig. 3. Analysis domain and sampling plan of the Wufeng, Taiwan, site

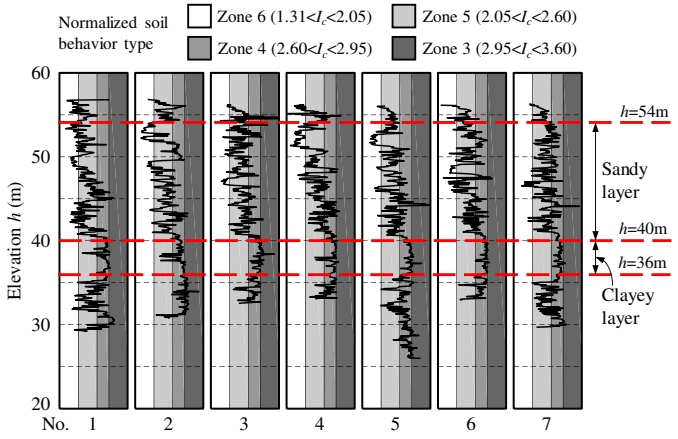

Fig. 4. Normalized soil behavior type and soil layer identification

0.5 s using Eq. (12) on a desktop computer with 16 GB RAM and one Intel Core i7 CPU clocked at 3.4 GHz.

As for 3D spatial interpolation, the kriging approach is commonly used in geotechnical practice (Samui and Sitharam 2010; Firouzianbandpey et al. 2015; Li et al. 2016c; Xiao et al. 2017b), with mean and standard deviation estimated as (Forrester et al. 2008)

$$\mathrm{E}(\boldsymbol{X}_u) = \boldsymbol{F}_u\hat{\boldsymbol{\beta}} + \boldsymbol{R}_{us}\boldsymbol{R}_{ss}^{-1}(\boldsymbol{X}_s - \boldsymbol{F}_s\hat{\boldsymbol{\beta}}) \tag{13}$$

$$\mathrm{S}(\boldsymbol{X}_u) = \hat{\sigma}\sqrt{\mathrm{diag}(\boldsymbol{R}_{uu} - \boldsymbol{R}_{us}\boldsymbol{R}_{ss}^{-1}\boldsymbol{R}_{us}^{\mathrm{T}})} \tag{14}$$

where $\mathrm{E}(\cdot)$ and $\mathrm{S}(\cdot)$ = mean and standard deviation, respectively; subscripts s and u = sampled and unsampled locations, respectively; $\boldsymbol{R}_{ss}$, $\boldsymbol{R}_{uu}$, and $\boldsymbol{R}_{us}$ = correlation matrices based on Eq. (2), respectively, among sampled locations, unsampled locations, and between unsampled and sampled locations; and $\mathrm{diag}(\cdot)$ = vector formed by diagonal elements of a matrix. Admittedly, the number of unsampled locations is usually much larger than that of sampled locations, leading to more serious computational difficulty in implementing Eqs. (13) and (14). Efficient 3D spatial interpolation is still possible if the concerned domain is a 3D lattice, as provided in Appendix III. The computational efficiency of both 3D spatial interpolation and 3D random field simulation benefits from the idea of decomposing the global correlation matrix as well.

Case Study: Wufeng, Taiwan, Site

For illustration, the MLE-based 3D spatial variability characterization approach was applied to a case study at Wufeng, Taiwan, which was investigated after the 1999 Chi-Chi earthquake (PEER 2003). The analysis domain was 60 × 50 m as shown in Fig. 3. Seven CPTs at a penetration interval of 50 mm were selected and processed following the procedure proposed by Fenton (1999b). According to Robertson (2009), the normalized soil behavior type index (I_c) was evaluated based on the normalized CPT data (i.e., Q_{tn} and F_r), as shown in Fig. 4, and then used to determine soil types with the updated Robertson's chart. The soil layer located from 40–54 m in elevation and the one from 36 to 40 m were identified as a sandy layer and a clayey layer, respectively. The identification of soil stratification in this study was not rigorous, without the consideration of the CPT transition zone from one soil layer to another (Robertson 2009) and a few embedded soil zones. The uncertainties from transition zones and embedded zones were viewed as part of the overall spatial variability being characterized.

The linear trend function $X = \beta_0 + \beta_z z$, where z = relative depth from the top of each soil layer, considered in this example has five random field parameters $\boldsymbol{\theta} = (\beta_0, \beta_z, \sigma, \delta_v, \delta_h)$ to identify. The optimization of the profile likelihood function [i.e., Eq. (6)] with respect to δ_v and δ_h is shown in Fig. 5, where circles and crosses represent random initial values and located global maxima, respectively. Table 2 summarizes the characterization results of all random field parameters for Q_{tn} and F_r in both soil layers. Taking soil properties in the middle of each soil layer as a reference, the COV values of Q_{tn} and F_r in the sandy layer and those in the clayey layer were 0.59 and 0.58, and 0.43 and 0.24, respectively, indicating that the sandy soils had a larger inherent variability than the clayey soils. The statistical uncertainty for random field parameters estimated by Eq. (10) is also given in Table 2. It was found that statistical uncertainties for β_0 and σ were minimal, with COV less than 0.1, while those for β_z and δ_h were typically larger than 0.3. Owing to the presence of a thin layer, random field parameters of clayey soils basically have larger statistical uncertainty than those of sandy soils. Regarding the 3D spatial variability, δ_h (i.e., from 5.36 to 11.19 m) was approximately one to two orders of magnitude larger than δ_v (i.e., from 0.16 to 0.77 m) for all soil properties,

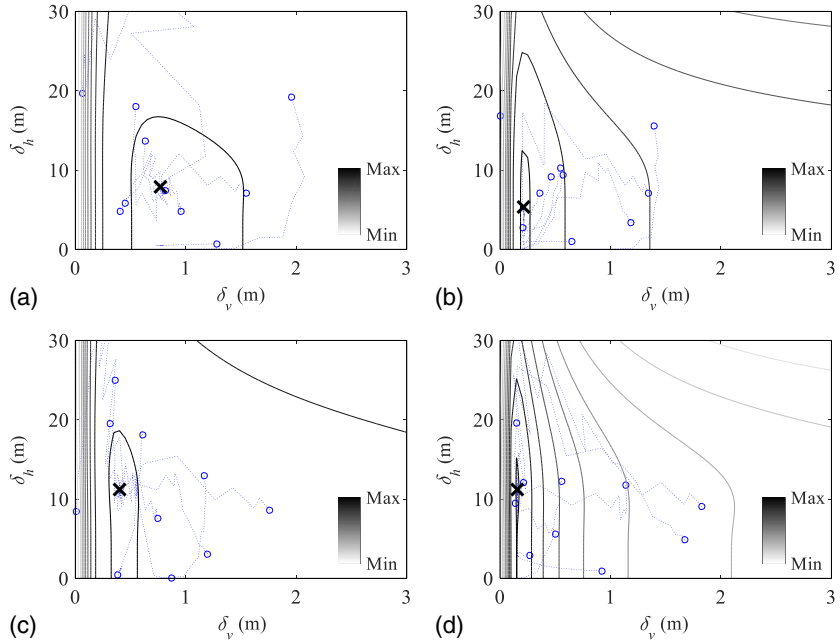

Fig. 5. Optimization of profile likelihood function in MLE: (a) sandy layer, Q_{tn}; (b) sandy layer, F_r; (c) clayey layer, Q_{tn}; (d) clayey layer, F_r

Table 2. Results of 3D Spatial Variability Characterization for the Wufeng, Taiwan, Site

Layer	CPT parameter	Method	β_0	β_z	σ	δ_v	δ_h
Sandy layer	Q_{tn}	MLE	87.61 (0.08)	−2.86 (−0.29)	39.80 (0.04)	0.77 (0.09)	7.86 (0.32)
		MMBF	88.37	−2.78	40.04	0.63	13.65
	F_r	MLE	2.76 (0.06)	0.06 (0.33)	1.83 (0.02)	0.22 (0.06)	5.36 (1.40)
		MMBF	2.76	0.06	1.83	0.47	9.13
Clayey layer	Q_{tn}	MLE	19.07 (0.08)	−1.38 (−0.49)	7.09 (0.06)	0.40 (0.13)	11.19 (0.33)
		MMBF	19.21	−1.43	7.28	0.36	24.99
	F_r	MLE	4.12 (0.03)	−0.39 (−0.13)	0.81 (0.04)	0.16 (0.11)	11.16 (0.27)
		MMBF	4.12	−0.39	0.81	0.15	19.55

Note: Values in parentheses are COV values for parameters estimated by MLE; local coordinate system located at the top of each soil layer is adopted.

consistent with that reported by Phoon and Kulhawy (1999). The statistical uncertainty of δ_h (i.e., from 0.27 to 1.40) was also several times larger than that of δ_v (i.e., from 0.06 to 0.13). This was expected because the horizontal data pair was much scarcer than the vertical data pair in this example.

For comparison, MMBF with individual characterizations of vertical and horizontal spatial variabilities was also carried out as shown in Fig. 6. As implemented in Jaksa (1995), Stuedlein et al. (2012), and Firouzianbandpey et al. (2014), MMBF lacks a standardized procedure for parameter inference to a certain degree, particularly for δ_v and δ_h. In this study, for vertical spatial variability characterization, the estimated sample correlation was averaged over all soundings, and δ_v was determined by fitting the initial part with correlation coefficients exceeding Bartlett's limit (Uzielli et al. 2005), while the sample correlation was averaged over all depths for horizontal spatial variability characterization, and δ_h was determined by fitting the whole part. The inferred random field parameters from MMBF are also given in Table 2. In general, MMBF and MLE give nearly consistent estimates on β_0, β_z, and σ, but quite different values on δ_v and δ_h. The individual characterization manner and nonstandardized best-fitting procedure in MMBF cannot make full use of the information contained in data and would affect characterization results especially in the presence of limited data.

After the 3D spatial variability characterization, the kriging-based 3D spatial interpolation was used to extend the knowledge of soil properties to the whole site. Consider Q_{tn} of the sandy layer, for example. The concerned domain was comprised of $120 \times 100 \times 280 \approx 3.4 \times 10^6$ elements. Applying the efficient interpolation technique in Appendix III to Eqs. (13) and (14), it takes approximately 0.5 s to predict the mean and standard deviation of Q_{tn} in the sandy layer, as illustrated in Fig. 7, on a desktop computer with 16 GB RAM and one Intel Core i7 CPU clocked at 3.4 GHz. It is easy for geotechnical engineers to determine soil properties at any location of the site by understanding the 3D spatial variability. As shown in Fig. 7(b), the mapping uncertainty was naught at locations of CPTs, and approached the maximum (i.e., $\sigma = 39.8$) at locations whose horizontal distance to any CPT was approximately larger than δ_h. Also, the mapping uncertainty almost remained unchanged along the depth. This was because the CPT data are nearly continuous in the vertical direction so the mapping uncertainty in 3D space was mainly dominated by the sparse horizontal data pair. For the same reason, results of 3D spatial interpolation were more sensitive to δ_h than δ_v. In view of the large statistical uncertainty of δ_h in this example, it is always advantageous to utilize the result of 3D spatial interpolation with caution and more CPTs are desired for better understanding this site.

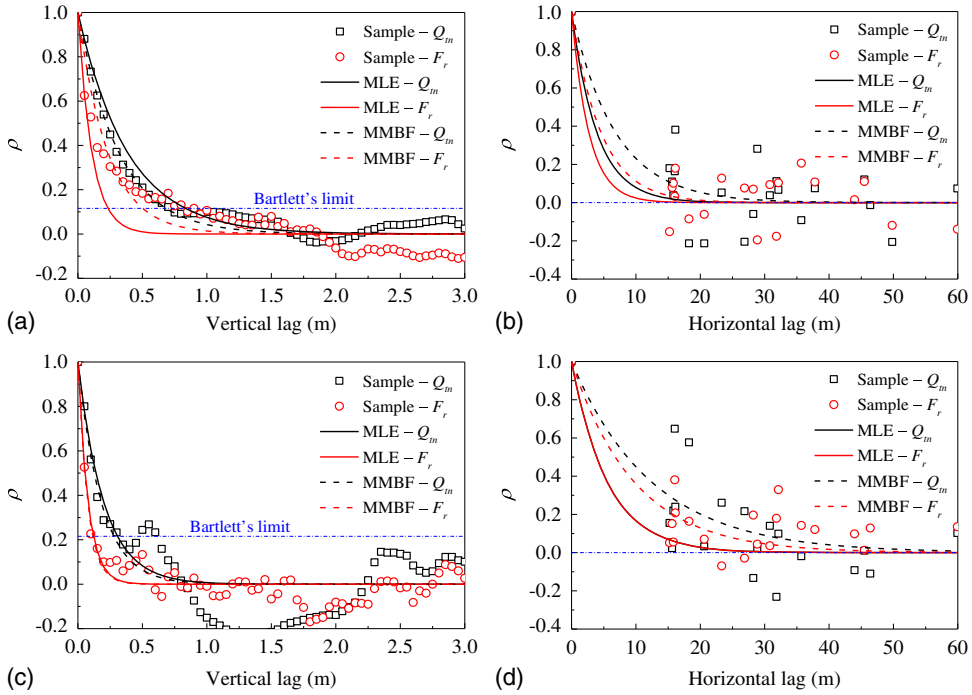

Fig. 6. Comparison of correlation functions: (a) sandy layer, vertical; (b) sandy layer, horizontal; (c) clayey layer, vertical; (d) clayey layer, horizontal

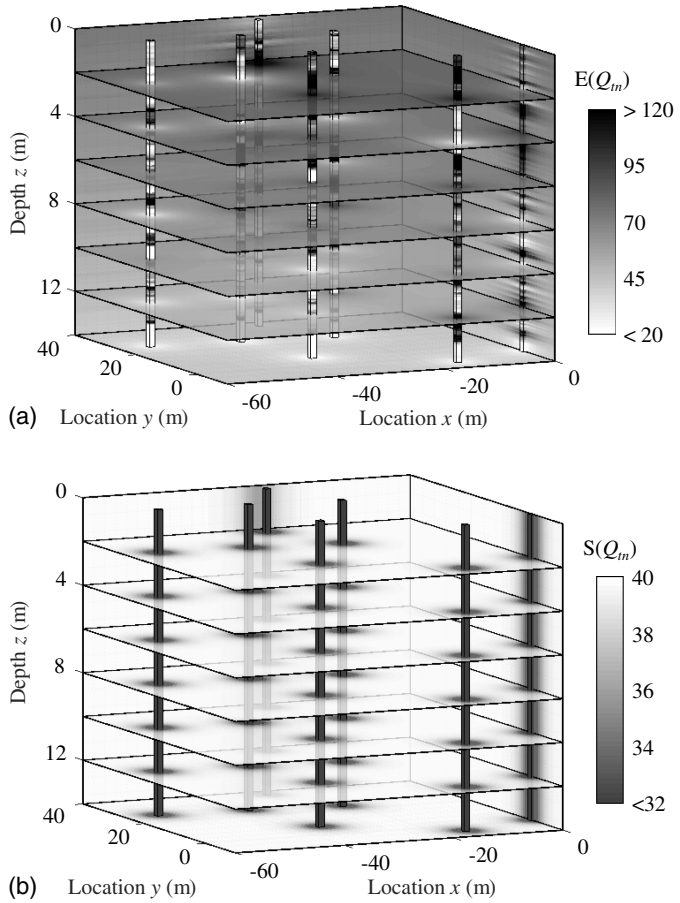

Fig. 7. Three-dimensional spatial interpolation for cone tip resistance of sandy layer: (a) mean; (b) standard deviation

Virtual Site Analysis

Actual soil properties were hardly known at a particular site, leaving results of 3D spatial variability characterization unverifiable. In order to validate the MLE-based 3D characterization approach and demonstrate its capabilities, this section implements several virtual site analyses as shown in Fig. 8. The procedure consists of two steps: (1) generating several sets (e.g., 100 sets in this study) of 3D spatially varying CPT data with prescribed random field parameters using the covariance matrix decomposition approach [i.e., Eq. (12)]; and (2) identifying random field parameters for each set of CPT data using MLE, and comparing against actual values and those obtained from MMBF as described in the case study. For convenience, all estimates were normalized by respective true values.

Example I: Relatively Sufficient Data

Recall the example in "Decomposition of Global Correlation Matrix." Forty CPTs at a penetration interval Δ_v of 20 mm and a depth of 20 m were simulated in a 1-km^2 virtual site, as shown in Fig. 8(a), with a 3D single-exponential correlation function [i.e., Eq. (2)], a 3D linear trend $X = \beta_0 + \beta_x x + \beta_y y + \beta_z z$, and $\boldsymbol{\theta} = (\beta_0, \beta_x, \beta_y, \beta_z, \sigma, \delta_v, \delta_h) = (100, 0.1, 0.1, 2, 40, 1, 20)$. These CPTs were collected for 3D spatial variability characterization in four phases, each of which contained 10 CPTs. The minimum sounding distance, between CPT-15 of Phase II and CPT-27 of Phase III, was approximately 8.6 m. The total numbers of used soundings in the four phases were 10, 20, 30, and 40, respectively, due to the collective utilization of all preceding CPTs.

By means of MLE, 100 sets of estimates and associated statistical uncertainties were obtained. The normalized mean and COV of estimates are illustrated in Figs. 9(a and b), respectively, among which the dotted and solid lines in Fig. 9(b) are the average of statistical uncertainty estimated by Eq. (10) and the direct COV

J. Geotech. Geoenviron. Eng., 2018, 144(5): 04018023

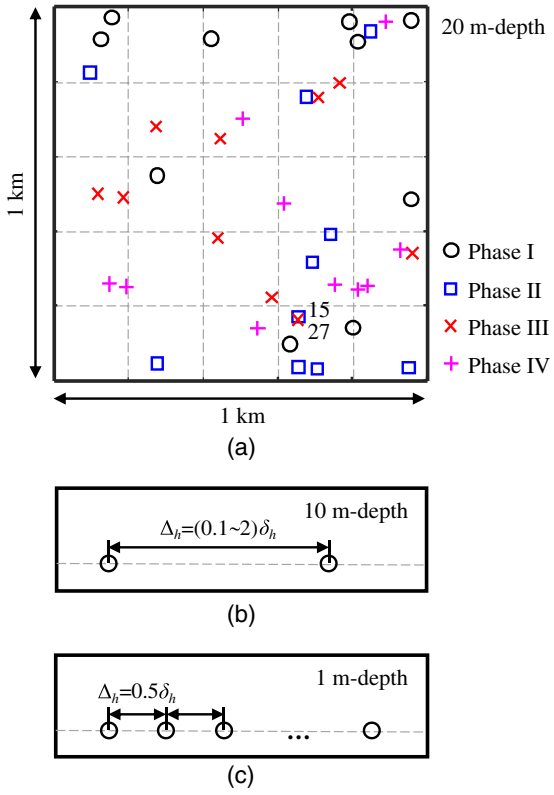

Fig. 8. Sampling plan for virtual site analysis: (a) Example I (relatively sufficient data); (b) Example II (limited sounding issue); (c) Example III (thin layer issue)

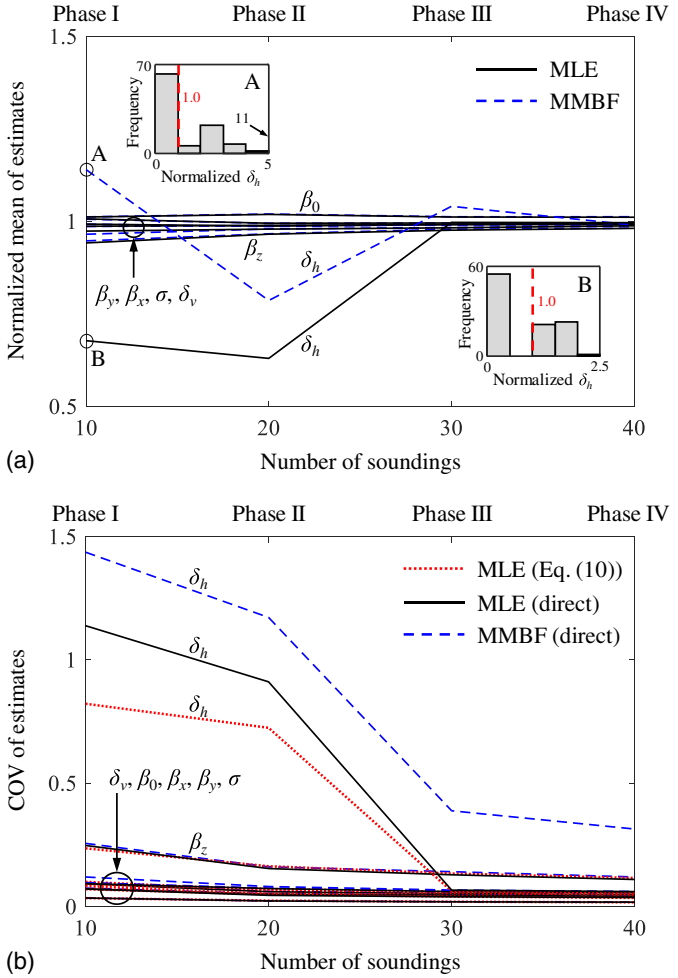

Fig. 9. Validation of 3D spatial variability characterization: (a) normalized mean of estimates (Insets A and B are frequencies of normalized δ_h in Phase I using MMBF and MLE, respectively); (b) COV of estimates

estimation based on 100 sets of estimates, respectively. The former agreed well with the latter, except for δ_h in Phases I and II. The inconsistency was attributed to the fact that δ_h was prone to be unidentifiable in the absence of sufficient data. Herein, unidentifiable δ_h means that δ_h had the same maximum likelihood in a wide range, normally including the zero as also observed in Xiao et al. (2017b), so that the optimization was likely to locate $\delta_h = 0$ [see Inset B in Fig. 9(a)]. Because MMBF cannot provide the quantified statistical uncertainty, the direct COV estimation was used for comparison between MLE and MMBF in the remaining part of this paper. As shown in Fig. 9(a), the normalized mean of δ_h converged to unity after Phase III (i.e., estimate comparable with the true value), while other random field parameters converged at the beginning. As more and more CPT data were employed, COV values of all parameters decreased from Phase I to Phase IV, as shown in Fig. 9(b), among which the COV of δ_h suddenly plunged from approximately 0.9 to less than 0.1 in Phase III. Besides, β_z had a larger statistical uncertainty than other parameters, even larger than δ_h after Phase III. All presented results validated the MLE-based 3D spatial variability characterization and showcased its ability to deal with high-dimensional data. Thanks to the matrix decomposition technique, a MLE with 40,000 readings in Phase IV required approximately 2.2 s on the desktop computer, which is efficient enough for practical applications.

Fig. 9 also presents the results obtained from MMBF. It is evident that, no matter the phase, the COV of δ_h from MMBF was much larger than that from MLE. When the number of CPT soundings was limited such as in Phase I, the estimate of δ_h oscillated between two extremes, namely, unidentifiable δ_h (i.e., $\delta_h = 0$) and extremely large δ_h (e.g., $\delta_h > 200$ m) [the second extreme occurs in MMBF only, see Insets A and B in Fig. 9(a)]. This phenomenon resulted from the best fitting for a small sample correlation (i.e., close to naught) at a large minimum distance, in which δ_h was probably enormous if the sample correlation was positive; otherwise, $\delta_h = 0$. Apart from δ_h, MMBF gave similar estimates for other parameters with slightly larger statistical uncertainty due to the relatively sufficient data in this example.

More capabilities of MLE-based 3D spatial variability characterization in the presence of limited data will be demonstrated in the following sections, including the limited sounding issue and the thin layer issue. For the sake of clarity, this paper does not argue that the limited data were acceptable for 3D spatial variability characterization, but advocates the need of using more advanced characterization methods (e.g., MLE with simultaneous vertical and horizontal spatial variability characterization) especially when data are inadequate.

Example II: Limited Sounding Issue

In reality, vertical and horizontal trends in normalized CPT data are typically small and hardly perceived by limited data. Hence, for simplicity, only a constant trend (i.e., β_0) is considered hereafter. Take an extreme scenario, namely, only two CPTs, for example. As shown in Fig. 8(b), two CPTs were performed with $\Delta_v = 50$ mm for 10-m depth, the horizontal distance Δ_h of which varies from

$0.1\delta_h$ to $2\delta_h$. Without loss of generality, soil properties are simulated with $\beta_0 = 100$, $\sigma = 40$, $\delta_v = (0.5, 1.0, 2.0)$ m, and $\delta_h = (10, 20, 40)$ m, leading to a total of nine cases.

Fig. 10 illustrates the function of normalized mean and COV for estimated parameters with different Δ_h values, in which solid and dashed lines denote characterization results using MLE and MMBF, respectively. Similar to Example I, estimates of β_0 and σ almost coincided using MLE and MMBF, and their normalized mean and COV values remained approximately unchanged (around unity and at a low level, respectively) with varying Δ_h. In contrast, the estimates of δ_v and δ_h had quite different trends in the presence of limited CPT soundings. On the one hand, in comparison with MMBF, δ_v and δ_h obtained by MLE were closer to respective true values, associated with smaller statistical uncertainties, and held better consistency for different cases. These indicate that MLE performs better than MMBF in the absence of sufficient data. On the other hand, Δ_h affected the estimation of δ_v and δ_h significantly with a turning point at one δ_h. Take the estimate of δ_h using MLE as an example. As Δ_h increased from $0.1\delta_h$ to δ_h, it fluctuated around the true value for all nine cases and its COV slowly rose from approximately 0.15 to approximately 0.35, still at an acceptable low level; however, as Δ_h exceeded δ_h, it deviated from the true value and suffered a dramatic increase in COV (e.g., approximately 1.0 for $\Delta_h = 2\delta_h$). This implied that a small sounding distance (i.e., $\Delta_h < \delta_h$) facilitated the 3D spatial variability characterization, particularly for scales of fluctuation. It is rational because the spatial correlation for two positions separated by more than one scale of fluctuation is almost negligible and unidentifiable. Unlike the problem of large sampling interval in the vertical direction (i.e., $\Delta_v > \delta_v$) that is avoided by CPT, the problem of large sounding distance should be bypassed through a well-designed sampling strategy.

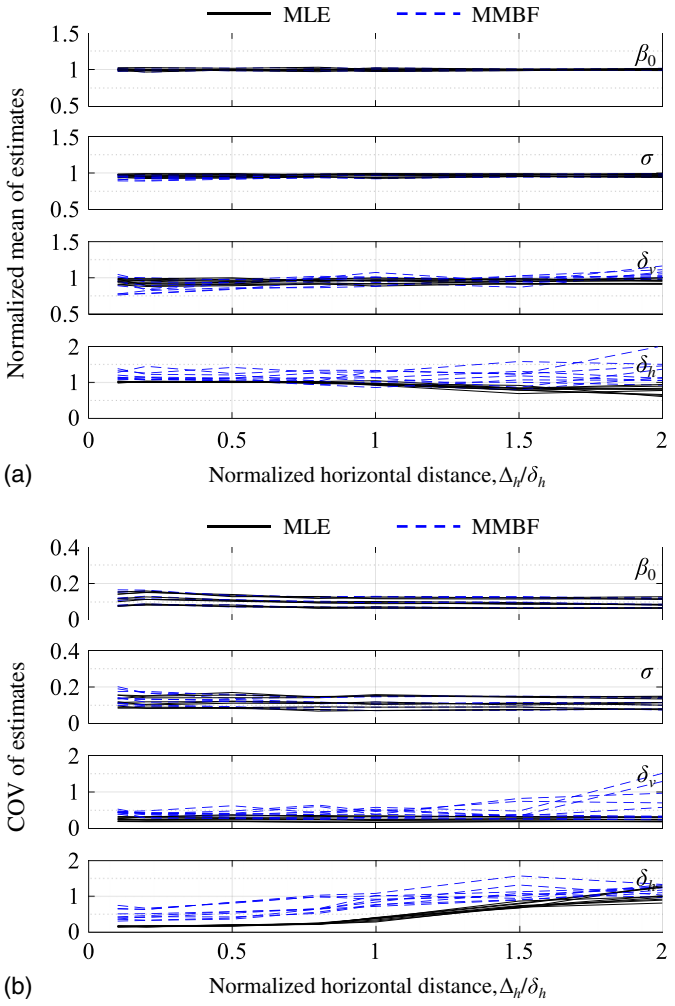

Fig. 10. Effect of horizontal distance for limited sounding issue: (a) normalized mean of estimates; (b) COV of estimates

Table 3. Results for Example I Based on 12 CPTs

Result	Method	β_0	β_x	β_y	β_z	σ	δ_v	δ_h
Normalized mean	MLE	1.01	0.99	1.00	0.96	0.99	0.98	1.00
	MMBF	1.01	0.99	1.00	0.97	0.99	0.97	1.13
COV	MLE[a]	0.09	0.09	0.07	0.22	0.03	0.06	0.07
	MLE[b]	0.09	0.09	0.07	0.21	0.03	0.06	0.07
	MMBF[b]	0.09	0.10	0.07	0.22	0.03	0.11	0.59

[a]Average of statistical uncertainty estimated by Eq. (10).
[b]Direct COV estimation based on 100 sets of estimates.

To further illustrate the importance of sampling strategy, the calculations in Example I were repeated using 12 CPTs only, namely 10 CPTs of Phase I, CPT-15 of Phase II, and CPT-27 of Phase III, and the results are summarized in Table 3. The results of MLE, including both normalized mean and COV, based on 12 CPTs were much better than those based on 10 CPTs (i.e., Phase I in Fig. 9) and comparable with those based on 30 CPTs (i.e., Phase III in Fig. 9). Again, this benefited from the fact that the two additional CPTs (i.e., CPT-15 and CPT-27) were closely located with $\Delta_h < \delta_h$. Therefore, in spite of unknown δ_h in reality, the sampling strategy of having some closely located CPTs is always preferable for 3D spatial variability characterization. Such a sampling strategy is also referred to as nested sampling (DeGroot and Baecher 1993).

Example III: Thin Layer Issue

The thin layer issue is another form of limited data issue and has been discussed by Ching et al. (2016b) in vertical spatial variability characterization. Despite inadequate CPT data within one single sounding as for a thin layer, the data collected from multiple CPTs may be enough. Consider that, for example, a 1-m-deep thin layer with the same soil properties as Example II. A series of CPTs was distributed ideally along a straight line with $\Delta_h = 0.5\delta_h$, as shown in Fig. 8(c). This sampling strategy was used for demonstration and may not be the optimal one.

Results of 3D spatial variability characterization with different sounding numbers (i.e., from 2 to 10) are shown in Fig. 11. For all nine cases, MLE again gave much better estimates than MMBF in terms of both accuracy (i.e., normalized mean close to unity) and statistical uncertainty (i.e., small COV), particularly for scales of fluctuation. In the context of MLE, estimates of σ and δ_v were apparently biased based on two CPTs, with normalized mean values of 0.75–0.9 and 0.6–0.9, respectively. Instead, the estimate of δ_h was relatively accurate because $\Delta_h < \delta_h$ as designed. Even though δ_v may exceed the depth (i.e., statistically very thin layer), all estimates of the random field parameters would converge to respective true values with tolerable statistical uncertainties, as long as a sufficiently large number of CPTs are available (e.g., more than six). This indicates that involving multiple CPTs in 3D space is a feasible way to address the thin layer issue and this study provides a powerful tool for this task.

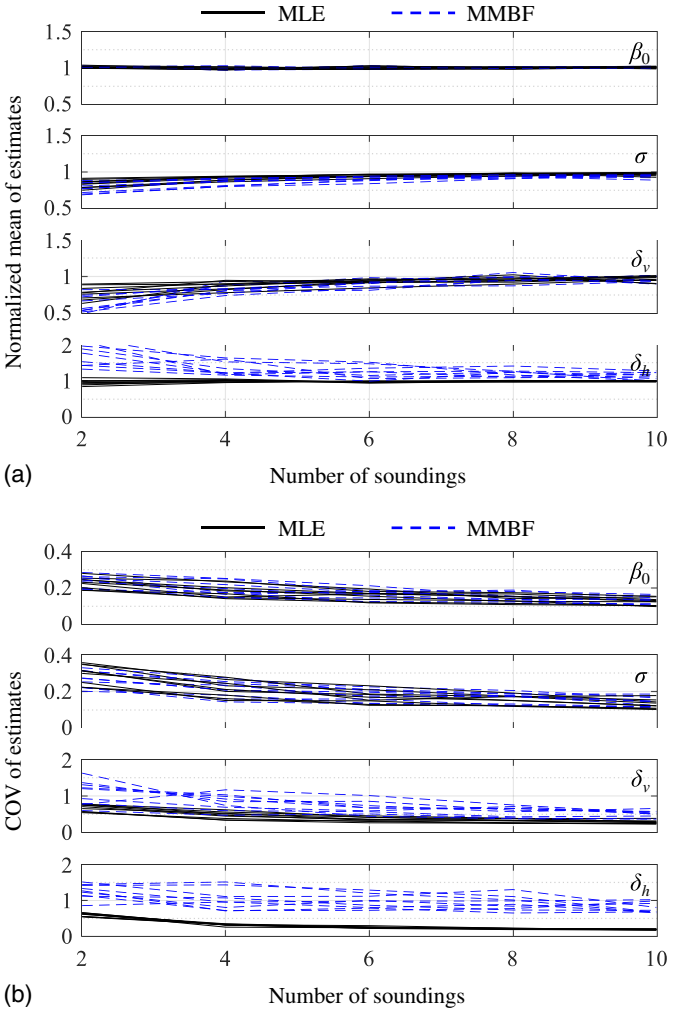

Fig. 11. Effect of sounding number for thin layer issue: (a) normalized mean of estimates; (b) COV of estimates

Discussion

As demonstrated in the preceding examples, 3D spatial variability characterization with simultaneous vertical and horizontal characterization could make full use of the information contained in limited data. It demands the participation of multiple CPTs and, in turn, creates a high-dimensional problem in MLE. In this paper, the problem is addressed by decomposing the large global correlation matrix into small vertical and horizontal correlation matrices with the aid of the Kronecker product. This idea also facilitates efficient 3D random field simulation and 3D spatial interpolation in a similar way.

The matrix decomposition technique works for particular sites, namely, those in homogeneous or horizontally stratified soils as shown in Figs. 1(a) and 4. As a matter of fact, such an ideal treatment is also required in conventional approaches for horizontal spatial variability characterization, such as Stuedlein et al. (2012) and Firouzianbandpey et al. (2014), although it may not be clarified explicitly. The 3D spatial variability characterization in more complex stratified soils (Xiao et al. 2017b) remains a nontrivial task and deserves more efforts in the future. Approximate MLE (Pardo-Igúzquiza and Dowd 1997; Stein et al. 2004) may be a good way. In addition, data completeness is also pivotal for the success of the matrix decomposition technique. Any missing data would make the global correlation matrix indecomposable. In order to remedy the missing data, a simple but practical CPT data processing procedure proposed by Fenton (1999b) is recommended. Specifically, if only a few readings at intermediate depths are missing (i.e., less than 5% of the total sounding), they can be interpolated between the previous and next existing records.

This study focuses on the parameter inference in probabilistic site characterization and the model comparison for different trend functions; probabilistic distributions and correlation functions were not considered. Interested readers may refer to Cao and Wang (2014), Tian et al. (2016), and Ching and Phoon (2017) for model comparison in probabilistic site characterization.

Summary and Conclusions

This study develops a CPT-based probabilistic approach for 3D spatial variability characterization, in which a matrix decomposition technique was applied to bypass the high-dimensional problem in MLE. Through the case study and virtual site analysis, the following conclusions can be drawn:

1. The matrix decomposition technique addresses the computational difficulty of MLE for high-dimensional and spatially correlated data and enhances the practical application of MLE in 3D spatial variability characterization with multiple CPTs. It also facilitates efficient 3D random field simulation and spatial interpolation to extend the knowledge from a few investigated locations to the whole site.
2. MLE provides more accurate estimates of random field parameters with smaller statistical uncertainty than the commonly used MMBF, particularly for the estimation of scale of fluctuation in the absence of sufficient data.
3. Simultaneous vertical and horizontal characterization based on multiple CPTs is a feasible way for 3D spatial variability characterization in the presence of limited data, such as the limited sounding issue and the thin layer issue. The sampling strategy having some closely located CPTs is preferable for 3D spatial variability characterization.
4. For the case study of the Wufeng, Taiwan, site, the sandy soils had a larger inherent variability than the clayey soils. The vertical and horizontal scales of fluctuation for both soils ranged from 0.16–0.77 m and from 5.36–11.19 m, respectively, and the horizontal scale of fluctuation had a larger statistical uncertainty than the vertical one.

Appendix I. Kronecker Product and Linear Matrix Equation

To save computational memory and improve computational efficiency, the Kronecker product for a large matrix can be converted as a linear matrix equation with several small matrices (Horn and Johnson 1991, Lemma 4.3.1). The lemma says that the matrix multiplication $\boldsymbol{D} = (\boldsymbol{A} \otimes \boldsymbol{B})\boldsymbol{C}$ with matrix sizes of $\boldsymbol{A}$, $\boldsymbol{B}$, $\boldsymbol{C}$, and $\boldsymbol{D}$ of $n_1 \times n_2$, $n_3 \times n_4$, $n_2 n_4 \times 1$, and $n_1 n_3 \times 1$, respectively, is equivalent to

$$\underline{\boldsymbol{D}} = \boldsymbol{B}\underline{\boldsymbol{C}}\boldsymbol{A}^{\mathrm{T}} \tag{15}$$

where $\underline{\boldsymbol{C}}$ and $\underline{\boldsymbol{D}}$ = reordered matrices of $\boldsymbol{C}$ and $\boldsymbol{D}$ with sizes of $n_4 \times n_2$ and $n_3 \times n_1$, respectively. Based on this lemma, the following identity exists:

$$\boldsymbol{D}^{\mathrm{T}}(\boldsymbol{A} \otimes \boldsymbol{B})\boldsymbol{C} = \mathrm{tr}(\underline{\boldsymbol{D}}^{\mathrm{T}}\boldsymbol{B}\underline{\boldsymbol{C}}\boldsymbol{A}^{\mathrm{T}}) \tag{16}$$

The lemma is very useful for efficient 3D spatial variability characterization, random field simulation, and spatial interpolation with high-dimensional data.

Appendix II. Second-Order Partial Derivatives of Log-Likelihood Function

For the log-likelihood function defined in Eq. (3), second-order partial derivatives with respect to $\boldsymbol{\beta}$ and σ are derived as

$$\frac{\partial^2 \ln L(\boldsymbol{X}|\boldsymbol{\theta})}{\partial \boldsymbol{\beta}^2} = -\frac{1}{\hat{\sigma}^2}\boldsymbol{F}^{\mathrm{T}}(\boldsymbol{H} \otimes \boldsymbol{V})\boldsymbol{F} \tag{17}$$

$$\frac{\partial^2 \ln L(\boldsymbol{X}|\boldsymbol{\theta})}{\partial \sigma^2} = -\frac{2n}{\hat{\sigma}^2} \tag{18}$$

$$\frac{\partial^2 \ln L(\boldsymbol{X}|\boldsymbol{\theta})}{\partial \boldsymbol{\beta}\partial \sigma} = -\frac{2}{\hat{\sigma}^3}\boldsymbol{F}^{\mathrm{T}}(\boldsymbol{H} \otimes \boldsymbol{V})\boldsymbol{E} \tag{19}$$

where $\boldsymbol{H} = \boldsymbol{R}_h^{-1}|_{\hat{\delta}_h}$; and $\boldsymbol{V} = \boldsymbol{R}_v^{-1}|_{\hat{\delta}_v}$. Other second-order partial derivatives related to δ_v and δ_h require finite-difference approximation as

$$\begin{aligned}\frac{\partial^2 \ln L(\boldsymbol{X}|\boldsymbol{\theta})}{\partial \boldsymbol{\beta}\partial \delta_v} &= \frac{1}{2\Delta_{\delta_v}\hat{\sigma}^2}\boldsymbol{F}^{\mathrm{T}}(\boldsymbol{H} \otimes \boldsymbol{V}^-)\boldsymbol{E} \\ \frac{\partial^2 \ln L(\boldsymbol{X}|\boldsymbol{\theta})}{\partial \boldsymbol{\beta}\partial \delta_h} &= \frac{1}{2\Delta_{\delta_h}\hat{\sigma}^2}\boldsymbol{F}^{\mathrm{T}}(\boldsymbol{H}^- \otimes \boldsymbol{V})\boldsymbol{E}\end{aligned} \tag{20}$$

$$\begin{aligned}\frac{\partial^2 \ln L(\boldsymbol{X}|\boldsymbol{\theta})}{\partial \sigma\partial \delta_v} &= \frac{1}{2\Delta_{\delta_v}\hat{\sigma}^3}\boldsymbol{E}^{\mathrm{T}}(\boldsymbol{H} \otimes \boldsymbol{V}^-)\boldsymbol{E} \\ \frac{\partial^2 \ln L(\boldsymbol{X}|\boldsymbol{\theta})}{\partial \sigma\partial \delta_h} &= \frac{1}{2\Delta_{\delta_h}\hat{\sigma}^3}\boldsymbol{E}^{\mathrm{T}}(\boldsymbol{H}^- \otimes \boldsymbol{V})\boldsymbol{E}\end{aligned} \tag{21}$$

$$\begin{aligned}\frac{\partial^2 \ln L(\boldsymbol{X}|\boldsymbol{\theta})}{\partial \delta_v^2} &= -\frac{n_h C_v}{2\Delta_{\delta_v}^2} + \frac{n}{\Delta_{\delta_v}^2} - \frac{1}{2\Delta_{\delta_v}^2\hat{\sigma}^2}\boldsymbol{E}^{\mathrm{T}}(\boldsymbol{H} \otimes \boldsymbol{V}^+)\boldsymbol{E} \\ \frac{\partial^2 \ln L(\boldsymbol{X}|\boldsymbol{\theta})}{\partial \delta_h^2} &= -\frac{n_v C_h}{2\Delta_{\delta_h}^2} + \frac{n}{\Delta_{\delta_h}^2} - \frac{1}{2\Delta_{\delta_h}^2\hat{\sigma}^2}\boldsymbol{E}^{\mathrm{T}}(\boldsymbol{H}^+ \otimes \boldsymbol{V})\boldsymbol{E}\end{aligned} \tag{22}$$

$$\frac{\partial^2 \ln L(\boldsymbol{X}|\boldsymbol{\theta})}{\partial \delta_v\partial \delta_h} = -\frac{1}{8\Delta_{\delta_v}\Delta_{\delta_h}\hat{\sigma}^2}\boldsymbol{E}^{\mathrm{T}}(\boldsymbol{H}^- \otimes \boldsymbol{V}^-)\boldsymbol{E} \tag{23}$$

where Δ_{δ_h} and Δ_{δ_v} = difference intervals of δ_h and δ_v, respectively; $\boldsymbol{H}^{\pm} = \boldsymbol{R}_h^{-1}|_{\hat{\delta}_h+\Delta_{\delta_h}} \pm \boldsymbol{R}_h^{-1}|_{\hat{\delta}_h-\Delta_{\delta_h}}$; $\boldsymbol{V}^{\pm} = \boldsymbol{R}_v^{-1}|_{\hat{\delta}_v+\Delta_{\delta_v}} \pm \boldsymbol{R}_v^{-1}|_{\hat{\delta}_v-\Delta_{\delta_v}}$; $C_h = \ln|\boldsymbol{R}_h|_{\hat{\delta}_h+\Delta_{\delta_h}}| + \ln|\boldsymbol{R}_h|_{\hat{\delta}_h-\Delta_{\delta_h}}| - 2\ln|\boldsymbol{R}_h|_{\hat{\delta}_h}|$; and $C_v = \ln|\boldsymbol{R}_v|_{\hat{\delta}_v+\Delta_{\delta_v}}| + \ln|\boldsymbol{R}_v|_{\hat{\delta}_v-\Delta_{\delta_v}}| - 2\ln|\boldsymbol{R}_v|_{\hat{\delta}_v}|$. These computations can be further simplified using the lemma of Kronecker product (i.e., Appendix I).

Appendix III. Efficient Spatial Interpolation for 3D Lattice

If the concerned spatial interpolation domain is a 3D lattice, the correlation matrix–related components in Eqs. (13) and (14) can be rewritten, by virtue of the Kronecker product, as

$$\begin{aligned}\boldsymbol{R}_{us}\boldsymbol{R}_{ss}^{-1}\boldsymbol{E}_s &= [(\boldsymbol{R}_{h,us} \otimes \boldsymbol{R}_{v,us})(\boldsymbol{R}_{h,ss}^{-1} \otimes \boldsymbol{R}_{v,ss}^{-1})]\boldsymbol{E}_s \\ &= [(\boldsymbol{R}_{h,us}\boldsymbol{R}_{h,ss}^{-1}) \otimes (\boldsymbol{R}_{v,us}\boldsymbol{R}_{v,ss}^{-1})]\boldsymbol{E}_s \\ &= (\boldsymbol{R}_{v,us}\boldsymbol{R}_{v,ss}^{-1})\underline{\boldsymbol{E}}_s(\boldsymbol{R}_{h,us}\boldsymbol{R}_{h,ss}^{-1})^{\mathrm{T}}\end{aligned} \tag{24}$$

$$\begin{aligned}\mathrm{diag}(\boldsymbol{R}_{us}\boldsymbol{R}_{ss}^{-1}\boldsymbol{R}_{us}^{\mathrm{T}}) &= \mathrm{diag}[(\boldsymbol{R}_{h,us} \otimes \boldsymbol{R}_{v,us})(\boldsymbol{R}_{h,ss}^{-1} \otimes \boldsymbol{R}_{v,ss}^{-1}) \\ &\quad \times (\boldsymbol{R}_{h,us}^{\mathrm{T}} \otimes \boldsymbol{R}_{v,us}^{\mathrm{T}})] \\ &= \mathrm{diag}[(\boldsymbol{R}_{h,us}\boldsymbol{R}_{h,ss}^{-1}\boldsymbol{R}_{h,us}^{\mathrm{T}}) \otimes (\boldsymbol{R}_{v,us}\boldsymbol{R}_{v,ss}^{-1}\boldsymbol{R}_{v,us}^{\mathrm{T}})] \\ &= [\mathrm{diag}(\boldsymbol{R}_{h,us}\boldsymbol{R}_{h,ss}^{-1}\boldsymbol{R}_{h,us}^{\mathrm{T}})] \otimes [\mathrm{diag}(\boldsymbol{R}_{v,us}\boldsymbol{R}_{v,ss}^{-1}\boldsymbol{R}_{v,us}^{\mathrm{T}})]\end{aligned} \tag{25}$$

This allows efficient 3D spatial interpolation for a large number of unsampled locations.

Acknowledgments

This work was supported by the National Key R&D Program of China (Project No. 2017YFC1501301), the National Natural Science Foundation of China (Project Nos. 51579190, 51528901, and 51679174) and the Research Grants Council of the Hong Kong Special Administrative Region (Project No. 16202716). The first author wishes to thank the Department of Civil and Environmental Engineering, Hong Kong University of Science and Technology, for hosting his visit as an exchange Ph.D. student.

References

Akkaya, A. D., and Vanmarcke, E. H. (2003). "Estimation of spatial correlation of soil parameters based on data from the Texas A&M University NGES." *Probabilistic Site Characterization at the National Geotechnical Experimentation Sites (GSP 121)*, E. H. Vanmarcke and G. A. Fenton, eds., ASCE, Reston, VA, 29–40.

Baecher, G. B., and Christian, J. T. (2003). *Reliability and statistics in geotechnical engineering*, Wiley, Hoboken, NJ.

Baecher, G. B., Jaksa, M. B., Brooker, P. I., and Kaggwa, W. S. (1999). "Inaccuracies associated with estimating random measurement errors (discussions and closures)." *J. Geotech. Geoenviron. Eng.*, 10.1061/(ASCE)1090-0241(1999)125:1(79.2), 79–80.

Bombasaro, E., and Kasper, T. (2016). "Evaluation of spatial soil variability in the Pearl River Estuary using CPTU data." *Soils Found.*, 56(3), 496–505.

Cai, G., Lin, J., Liu, S., and Puppala, A. J. (2017). "Characterization of spatial variability of CPTU data in a liquefaction site improved by vibro-compaction method." *KSCE J. Civ. Eng.*, 21(1), 209–219.

Cao, Z., and Wang, Y. (2013). "Bayesian approach for probabilistic site characterization using cone penetration tests." *J. Geotech. Geoenviron. Eng.*, 10.1061/(ASCE)GT.1943-5606.0000765, 267–276.

Cao, Z., and Wang, Y. (2014). "Bayesian model comparison and selection of spatial correlation functions for soil parameters." *Struct. Saf.*, 49, 10–17.

Ching, J., and Phoon, K. K. (2017). "Characterizing uncertain site-specific trend function by sparse Bayesian learning." *J. Eng. Mech.*, 10.1061/(ASCE)EM.1943-7889.0001240, 04017028.

Ching, J., Phoon, K. K., and Wu, S. H. (2016a). "Impact of statistical uncertainty on geotechnical reliability estimation." *J. Eng. Mech.*, 10.1061/(ASCE)EM.1943-7889.0001075, 04016027.

Ching, J., Wu, S. S., and Phoon, K. K. (2016b). "Statistical characterization of random field parameters using frequentist and Bayesian approaches." *Can. Geotech. J.*, 53(2), 285–298.

DeGroot, D. J., and Baecher, G. B. (1993). "Estimating autocovariance of in-situ soil properties." *J. Geotech. Eng.*, 10.1061/(ASCE)0733-9410(1993)119:1(147), 147–166.

Fenton, G. A. (1999a). "Estimation for stochastic soil models." *J. Geotech. Geoenviron. Eng.*, 10.1061/(ASCE)1090-0241(1999)125:6(470), 470–485.

Fenton, G. A. (1999b). "Random field modeling of CPT data." *J. Geotech. Geoenviron. Eng.*, 10.1061/(ASCE)1090-0241(1999)125:6(486), 486–498.

Fenton, G. A., and Griffiths, D. V. (2008). *Risk assessment in geotechnical engineering*, Wiley, Hoboken, NJ.

Firouzianbandpey, S., Griffiths, D. V., Ibsen, L. B., and Andersen, L. V. (2014). "Spatial correlation length of normalized cone data in sand: Case study in the north of Denmark." *Can. Geotech. J.*, 51(8), 844–857.
Firouzianbandpey, S., Ibsen, L. B., Griffiths, D. V., Vahdatirad, M. J., Andersen, L. V., and Sørensen, J. D. (2015). "Effect of spatial correlation length on the interpretation of normalized CPT data using a Kriging approach." *J. Geotech. Geoenviron. Eng.*, 10.1061/(ASCE)GT.1943-5606.0001358, 04015052.
Forrester, A., Sobester, A., and Keane, A. (2008). *Engineering design via surrogate modelling: A practical guide*, Wiley, Chichester, U.K.
Horn, R. A., and Johnson, C. R. (1991). *Topics in matrix analysis*, Cambridge University Press, Cambridge, U.K.
Jaksa, M. B. (1995). "The influence of spatial variability on the geotechnical design properties of a stiff, overconsolidated clay." Ph.D. thesis, Univ. of Adelaide, Adelaide, Australia.
Kulatilake, P. H., and Miller, K. M. (1987). "A scheme for estimating the spatial variation of soil properties in three dimensions." *Proc., 5th Int. Conf. on Applications of Statistics and Probability in Soil and Structural Engineering (ICASP5)*, Univ. of Waterloo, Waterloo, ON, Canada, 669–677.
Lacasse, S., and Nadim, F. (1996). "Uncertainties in characterising soil properties." *Uncertainty in the Geologic Environment: From Theory to Practice (GSP 58)*, C. D. Shackleford, et al., eds., ASCE, Reston, VA, 49–75.
Li, D. Q., Xiao, T., Cao, Z. J., Phoon, K. K., and Zhou, C. B. (2016a). "Efficient and consistent reliability analysis of soil slope stability using both limit equilibrium analysis and finite element analysis." *Appl. Math. Model.*, 40(9), 5216–5229.
Li, D. Q., Xiao, T., Cao, Z. J., Zhou, C. B., and Zhang, L. M. (2016b). "Enhancement of random finite element method in reliability analysis and risk assessment of soil slopes using subset simulation." *Landslides*, 13(2), 293–303.
Li, J., Cassidy, M. J., Huang, J., Zhang, L., and Kelly, R. (2016c). "Probabilistic identification of soil stratification." *Géotechnique*, 66(1), 16–26.
Lingwanda, M. I., Prästings, A., Larsson, S., and Nyaoro, D. L. (2017). "Comparison of geotechnical uncertainties linked to different soil characterization methods." *Geomech. Geoeng.*, 12(2), 137–151.
Liu, C. N., and Chen, C. H. (2006). "Mapping liquefaction potential considering spatial correlations of CPT measurements." *J. Geotech. Geoenviron. Eng.*, 10.1061/(ASCE)1090-0241(2006)132:9(1178), 1178–1187.
Liu, C. N., and Chen, C. H. (2010). "Spatial correlation structures of CPT data in a liquefaction site." *Eng. Geol.*, 111(1–4), 43–50.
Lloret-Cabot, M., Fenton, G. A., and Hicks, M. A. (2014). "On the estimation of scale of fluctuation in geostatistics." *Georisk*, 8(2), 129–140.
Müller, R., Larsson, S., and Spross, J. (2013). "Extended multivariate approach for uncertainty reduction in the assessment of undrained shear strength in clays." *Can. Geotech. J.*, 51(3), 231–245.
Ng, I. T., and Zhou, C. Y. (2010). "Uncertainty-based optimization of site characterization using CPT." *Proc., 2nd Int. Symp. on Cone Penetration Testing (CPT'10)*, CPT'10 Organizing Committee, Huntington Beach, CA, 1–8.
O'Neill, M. W., and Yoon, G. L. (2003). "Spatial variability of CPT parameters at University of Houston NGES." *Probabilistic Site Characterization at the National Geotechnical Experimentation Sites (GSP 121)*, E. H. Vanmarcke and G. A. Fenton, eds., ASCE, Reston, VA, 1–12.
Pardo-Igúzquiza, E., and Dowd, P. A. (1997). "AMLE3D: A computer program for the inference of spatial covariance parameters by approximate maximum likelihood estimation." *Comput. Geosci.*, 23(7), 793–805.
Pawitan, Y. (2001). *In all likelihood: Statistical modelling and inference using likelihood*, Oxford University Press, Oxford, U.K.
PEER (Pacific Earthquake Engineering Research Center). (2003). "Wufeng-Site C." ⟨http://peer.berkeley.edu/lifelines/research_projects/3A02/wufeng-site-c.html⟩ (Jan. 1, 2017).
Phoon, K. K. (2017). "Role of reliability calculations in geotechnical design." *Georisk*, 11(1), 4–21.
Phoon, K. K., and Kulhawy, F. H. (1999). "Characterization of geotechnical variability." *Can. Geotech. J.*, 36(4), 612–624.
Phoon, K. K., Kulhawy, F. H., and Grigoriu, M. D. (1995). "Reliability-based design of foundations for transmission line structures." *Rep. TR-105000*, Electric Power Research Institute, Palo Alto, CA.
Robertson, P. K. (2009). "Interpretation of cone penetration tests: A unified approach." *Can. Geotech. J.*, 46(11), 1337–1355.
Samui, P., and Sitharam, T. G. (2010). "Site characterization model using artificial neural network and kriging." *Int. J. Geomech.*, 10.1061/(ASCE)1532-3641(2010)10:5(171), 171–180.
Stein, M. L., Chi, Z., and Welty, L. J. (2004). "Approximating likelihoods for large spatial data sets." *J. R. Stat. Soc. Ser. B-Stat. Methodol.*, 66(2), 275–296.
Stuedlein, A. W., Kramer, S. L., Arduino, P., and Holtz, R. D. (2012). "Geotechnical characterization and random field modeling of desiccated clay." *J. Geotech. Geoenviron. Eng.*, 10.1061/(ASCE)GT.1943-5606.0000723, 1301–1313.
Tang, W. H. (1979). "Probabilistic evaluation of penetration resistances." *J. Geotech. Eng. Div.*, 105(10), 1173–1191.
Tian, M., Li, D. Q., Cao, Z. J., Phoon, K. K., and Wang, Y. (2016). "Bayesian identification of random field model using indirect test data." *Eng. Geol.*, 210, 197–211.
Uzielli, M., Vannucchi, G., and Phoon, K. K. (2005). "Random field characterisation of stress-nomalised cone penetration testing parameters." *Géotechnique*, 55(1), 3–20.
Vanmarcke, E. H. (2010). *Random fields: Analysis and synthesis: Revised and expanded new edition*, World Scientific Publishing, Singapore.
Vrouwenvelder, T., and Calle, E. (2003). "Measuring spatial correlation of soil properties." *Heron*, 48(4), 297–311.
Wang, Y., Au, S. K., and Cao, Z. (2010). "Bayesian approach for probabilistic characterization of sand friction angles." *Eng. Geol.*, 114(3), 354–363.
Wang, Y., Cao, Z., and Li, D. (2016). "Bayesian perspective on geotechnical variability and site characterization." *Eng. Geol.*, 203, 117–125.
Wu, T. H., Lee, I. M., Potter, J. C., and Kjekstad, O. (1987). "Uncertainties in evaluation of strength of marine sand." *J. Geotech. Eng.*, 10.1061/(ASCE)0733-9410(1987)113:7(719), 719–738.
Xiao, T., Li, D. Q., Cao, Z. J., Au, S. K., and Phoon, K. K. (2016). "Three-dimensional slope reliability and risk assessment using auxiliary random finite element method." *Comput. Geotech.*, 79, 146–158.
Xiao, T., Li, D. Q., Cao, Z. J., and Tang, X. S. (2017a). "Full probabilistic design of slopes in spatially variable soils using simplified reliability analysis method." *Georisk*, 11(1), 146–159.
Xiao, T., Zhang, L. M., Li, X. Y., and Li, D. Q. (2017b). "Probabilistic stratification modeling in geotechnical site characterization." *ASCE-ASME J. Risk Uncertainty Eng. Syst., Part A: Civ. Eng.*, 10.1061/AJRUA6.0000924, 04017019.
Zhang, L. M., and Dasaka, S. M. (2010). "Uncertainties in geologic profiles versus variability in pile founding depth." *J. Geotech. Geoenviron. Eng.*, 10.1061/(ASCE)GT.1943-5606.0000364, 1475–1488.